Front. Phys. 11(6), 114205 (2016)
DOI 10.1007/s11467-016-0576-3

RESEARCH ARTICLE

Optical processes of photonic band gap structure with dressing field in atomic system

Yun-Zhe Zhang (张云哲)[1,2], Zhe Liu (刘哲)[2], Kang-Ning Cai (蔡康宁)[1], Hua Zhong (钟华)[1], Wei-Tao Zhang (张卫涛)[2], Jun-Feng Liu (刘俊锋)[1], Yan-Peng Zhang (张彦鹏)[1,†]

[1] *Key Laboratory for Physical Electronics and Devices of the Ministry of Education & Shaanxi Key Lab of Information Photonic Technique, Xi'an Jiaotong University, Xi'an 710049, China*
[2] *Institue of Applied Physics, Xi'an University, Xi'an 710065, China*
Corresponding author. E-mail: [†] *ypzhang@mail.xjtu.edu.cn*

Received January 16, 2016; accepted March 4, 2016

We experimentally investigate probe transmission signals (PTS), the four-wave mixing photonic band gap signal (FWM BGS), and the fluorescence signal (FLS) in an inverted Y-type four level atomic system. For the first time, we compare the FLS of the two ground-state hyperfine levels of Rb 85. In particular, the second-order and the fourth-order fluorescence signals perform dramatic dressing discrepancies under the two hyperfine levels. Moreover, we find that the dressing field has some dressing effects on three such types of signals. Therefore, we demonstrate that the characteristics of PTS, FWM BGS, and FLS can be controlled by frequency detunings, the powers or phases of the dressing field. Such research could have potential applications in optical diodes, amplifiers, and quantum information processing.

Keywords four-wave mixing, electromagnetically induced transparency, photonic band gap

PACS numbers 42.50.Gy, 42.65.An, 42.70.Qs

1 Introduction

Recently, electromagnetically induced transparency (EIT) [1, 2] has attracted worldwide attention in relation to atomic coherence in a hot atomic medium, and it can be used in multi-wave-mixing processes. It is widely known that the four-wave mixing (FWM) process [3] can emerge from three light fields under the EIT condition, and the FWM signals can be enhanced or suppressed in multilevel atomic systems [4], so the nonlinear optical properties can obviously be modified. These changes may have some potential applications in quantum communication [5, 6]. Usually, FWM is used in a fiber for generating new lasers in optical communications [7–9]. Furthermore, two coupling light fields with the same frequency will form standing waves (SWs) in a FWM process [10, 11], which is usually called electromagnetically induced grating (EIG) [12–15]. Moreover, the EIG possesses a photonic band gap (PBG) structure can reflect the probe light field [16, 17]. This research can also be used to fabricate optical diodes. When light is transmitted through structure if its frequency is outside the gap, but it is not transmitted if the frequency is inside the gap. Due to the Doppler effect, the counter propagating light is blue shifted and the co-propagating light is red shifted in the reference frame of the moving photonic gap. If only one of the shifted frequencies is within the gap, an optical diode is formed [18]. It is important to note that the PBG in a FWM process has many applications in several fields, such as all-optical switches [18], light storage [19], slow light generation [20], and optically controlled higher-order nonlinear fluorescence (FL) [21].

In this paper, we simultaneously compare the probe transmission signals (PTS), four-wave mixing (FWM), and fluorescence signals (FLS) under dressing effects in a reverted Y-type atomic system. We first observe the PBG structure based on an EIT medium driven by a SW field. The EIT peaks in the PTS, the suppression dips in FWM BGS, and the fluorescence peaks in FLS can be observed when we scan the dressing field frequency detuning. For the first time, we find that some dramatic dressing differences can be observed between the second order and fourth-order FLS under different hyperfine levels. Then, we can modulate the intensity and shape of these three signals through changing the powers of the dressing field in the EIG. Finally, the EIT and electromagnetically induced absorption (EIA) switching in PTS and the suppression and the width of FWM BGS can also be controlled by the phase of the dressing field. This information may be useful for the modulation of the signals, which highlights the significance of this research work. This paper is structured as follows: In Section 2, we describe the experimental setup and the corresponding theoretical model. In Section 3, we discuss the experimental results in detail, and in Section 4, we present our conclusions.

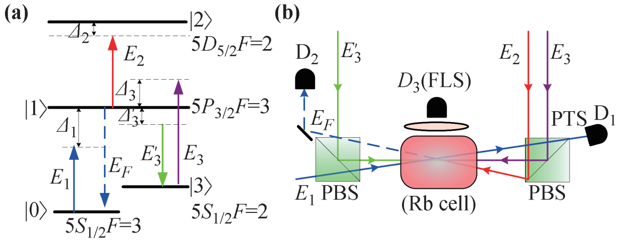

Fig. 1 **(a)** Four-level energy system. **(b)** Schematic of an EIG formed by two coupling beams E_3 and E_3', together with the dressing beam E_2, a FWM BGS will be generated according to the phase-matching condition $\boldsymbol{k}_{\mathrm{F}} = \boldsymbol{k}_1 + \boldsymbol{k}_3 - \boldsymbol{k}_3'$.

2 Experimental setup and theoretical model

Our experiment was carried out in a rubidium (^{85}Rb) atomic vapor cell. The 10 cm long rubidium cell is wrapped with a μ-metal and heated by heater tape, and the atom density is about 1.0×10^{12}cm^{-3}. The relevant energy levels for ^{85}Rb atoms are shown in Fig. 1(a). This is an inverse Y-type system with five levels, and the corresponding energy levels are $|0\rangle(5S_{1/2})$, $|3\rangle(5S_{1/2})$, $|1\rangle(5P_{3/2})$, and $|2\rangle(5D_{3/2})$. This experimental configuration with four laser beams was displayed as shown in Fig. 1(b). Initially, as displayed in Fig. 1(a), the probe laser beam E_1 (wave vector $\boldsymbol{k}_1$, frequency ω_1) probes the transition from $|0\rangle$ to $|1\rangle$, and the wavelength is about 780 nm. A pair of coupling beams $E_3(\boldsymbol{k}_3, \omega_3)$ and $E_3'(\boldsymbol{k}_3', \omega_3')$ connect the transition from $|3\rangle$ to $|1\rangle$ with a vertical polarization. Particularly, they have the same wavelength of about 780.238 nm. Moreover, another dressed beam $E_2(\boldsymbol{k}_2, \omega_2)$ connects the transition from $|1\rangle$ to $|2\rangle$ with a vertical polarization and the wavelength is about 775.978 nm.

Furthermore, as shown in Fig. 1(b), the coupling fields E_3 and E_3' propagate through the medium in the opposite direction generating a standing wave $E_{31} = \hat{y}[E_3\cos(\omega_3 t - k_3 x) + E_3'\cos(\omega_3' t + k_3' x)]$, i.e., EIG. Furthermore, this EIG will lead to a PBG structure. The probe field E_1 propagates in the same direction as E_3' through the medium with a small angle. The dressing field E_2 propagates in the opposite direction of E_3' with a small angle. When the probe field E_1 is incident from the left, in the system, the FWM BGS generated satisfies the phase-matching condition $\boldsymbol{k}_{\mathrm{F}} = \boldsymbol{k}_1 + \boldsymbol{k}_3 - \boldsymbol{k}_3'$ in Fig. 1(b). Using this experiment setup, we will investigate three types of signals simultaneously: the PTS, FWM BGS, and FLS. These three kinds of signals are detected by three photodiodes: D_1, D_2, and D_3, respectively.

Theoretically, according to the perturbation chain $\rho_{00}^{(0)} \xrightarrow{\omega_1} \rho_{10}^{(1)} \xrightarrow{-\omega_3} \rho_{30}^{(2)} \xrightarrow{\omega_3} \rho_{10}^{(3)}$, we can obtain the first-order density matrix $\rho_{10}^{(1)}$ (related to PTS) and the third-order density matrix elements $\rho_{10}^{(3)}$ (related to FWM BGS) as

$$\rho_{10}^{(1)} = \mathrm{i}G_1/(d_1 + |G_{31}|^2/d_3 + |G_2|^2/d_2)^2, \tag{1}$$

$$\rho_{10}^{(3)} = -\mathrm{i}G_1G_3G_3'/[(d_1 + |G_{31}|^2/d_3 + |G_2|^2/d_2)^2 d_3], \tag{2}$$

where $d_1 = \Gamma_{10} + \mathrm{i}\Delta_1$, $d_2 = \Gamma_{20} + \mathrm{i}(\Delta_1 + \Delta_2)$, $d_3 = \Gamma_{30} + \mathrm{i}(\Delta_1 - \Delta_3)$ and $G_{31}|^2 = |G_3|^2 + |G_3'|^2 + 2G_3G_3'\cos(2k_3x)$. $G_i = \mu_i\boldsymbol{E}_i/h$ is the Rabi frequency with a transition dipole moment μ_i, frequency detuning $\Delta_i = \Omega_i - \omega_i$ (Ω_i is the resonance frequency of the transition driven by $\boldsymbol{E}_i$) and Γ_{ij} is transverse relaxation rate between $|i\rangle$ and $|j\rangle$. In addition, two types of fluorescence signals, falling into the EIT window due to spontaneous emission, are also obtained: the decay of photons from $|1\rangle$ to $|0\rangle$ generates the second-order FLS R_0 described by $\rho_{11}^{(2)} = -|G_1|^2/[\Gamma_{11}(d_1 + |G_2|^2/d_2 + |G_{31}|^2/d_3)]$ (Liouville pathway $\rho_{00}^{(0)} \xrightarrow{G_1} \rho_{10}^{(1)} \xrightarrow{(G_1)^*} \rho_{11}^{(2)}$), and the decay of photons from $|2\rangle$ to $|1\rangle$ generates the fourth-order FLS R_1 with respect to $\rho_{22}^{(4)} = |G_1|^2|G_2|^2/[\Gamma_{22}d_1d_4(d_2 + |G_2|^2/d_1)]$ and $d_4 = \Gamma_{21} + \mathrm{i}\Delta_2$ (Liouville pathway $\rho_{00}^{(0)} \xrightarrow{G_1} \rho_{10}^{(1)} \xrightarrow{G_2} \rho_{20}^{(2)} \xrightarrow{(G_1)^*} \rho_{21}^{(3)} \xrightarrow{(G_2)^*} \rho_{22}^{(4)}$).

The condition of generating a PBG structure is that the medium should have a periodic refractive index (n). In order to get the periodic refractive index, the susceptibility should also be periodic as defined by the relation $n = \sqrt{1 + \mathrm{Re}\,(\chi)}$. Further, we may generate the periodic energy level structure for obtaining the periodic susceptibility. Hence, by introducing a periodic standing wave field, we can obtain the periodic energy levels as shown in Fig. 2. In Figs. 2(a1)–(a3), the level $|1\rangle$ will be split into two dressed states $|G_{3s\pm}\rangle$ depending on Δ_3 and $|G_{3s}|^2$. The two dressed states $|G_{3s\pm}\rangle$ have Eigenvalues $\lambda_{|G_{3\pm}\rangle} = -\Delta_3/2 \pm \sqrt{\Delta_3^2/4 + |G_{31}|^2}$. Since $|G_{31}|^2$ is periodic along the x-axis, $\lambda_{|G_{3\pm}|}$ values are also periodic along x. Thus we can obtain the periodic energy levels as shown in Figs. 2(b1)–(b3). In Fig. 2(b1), when $\Delta_3 < 0$, we have the Eigenvalues $\lambda_{|G_{3+}\rangle} > 0$ and $\lambda_{|G_{3-}\rangle} < 0$ as $\Delta_3 < 0$, so the split level $|G_{3s+}\rangle$ is lo-

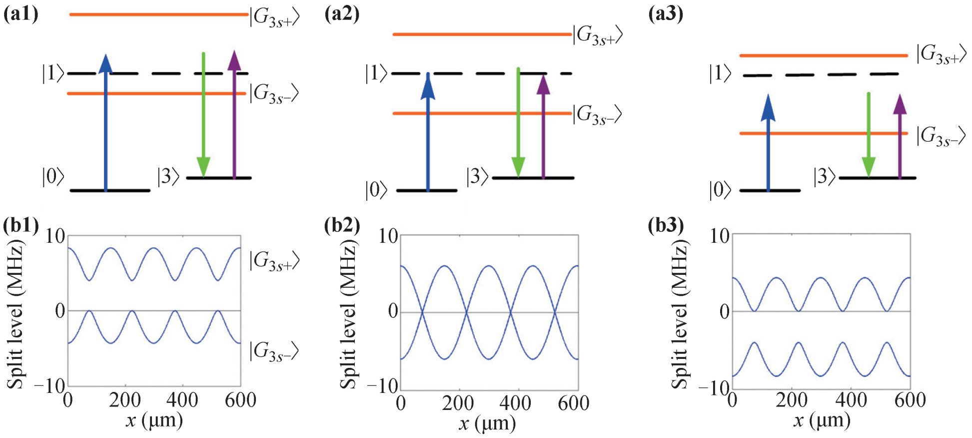

Fig. 2 **(a1–a3)** single dressed energy level schematic diagrams and **(b1–b3)** calculated single dressed period energy levels with changing $\varDelta_3$.

cated at the upper side of zero calibration (y-axis) while the level $|G_{3s-}\rangle$ is located at the lower side. Absorption will be enhanced when the probe resonates with the dressing states, i.e., $\varDelta_1 = -\lambda_{|G_{3\pm}\rangle}$, which corresponds to the EIA condition. Accordingly, the FWM signal will be enhanced. Figure 2(b2) shows that when the probe reaches two-photon resonance $\varDelta_1 - \varDelta_3 = 0$, absorption will be suppressed, i.e., the PTS becomes strong. Simultaneously, the FWM BGS will be correspondingly suppressed. Thus, $\varDelta_1 - \varDelta_3 = 0$ is defined as the suppression condition. Lastly, the case in Fig. 2(b3) is opposite to that in Fig. 2(b1) because $\varDelta_3 > 0$.

3 Results and discussion

First of all, with the beams $\boldsymbol{E}_1$, $\boldsymbol{E}_2$, $\boldsymbol{E}_2$, and E_3' turned on, we study the variations of PTS, FWM BGS, and FLS with the dressing effect ($\boldsymbol{E}_2$) by scanning $\varDelta_2$ at different $\varDelta_1$, as shown in Figs. 3(a1)–(c1). First, for PTS [Fig. 3(a1)], the total profile (dashed curve) consisting of baselines shows a Doppler absorption background with a peak (named profile peak) on it, and the peak caused by the dressing effect of the field E_3 (satisfying $\varDelta_1 - \varDelta_3 = 0$) associated with the term $|G_{31}|^2/[\varGamma_{30} + \mathrm{i}(\varDelta_1 - \varDelta_3)]$ in the expression of $\rho_{10}^{(1)}$, which denotes that the transparency degree increases. In each sub curve, the EIT peaks higher than the baselines appear at $\varDelta_1 + \varDelta_2 = 0$, which is induced by the dressing field E_2 according to the dressing term $|G_2|^2/[\varGamma_{20} + \mathrm{i}(\varDelta_1 + \varDelta_2)]$ in $\rho_{10}^{(1)}$. The total EIT peak reaches the highest point at $\varDelta_1 = \varDelta_3 = -\varDelta_2 \approx 0$, which indicates that the transparency degree of the probe field E_1 is significantly enhanced due to the interaction between E_2 and E_3 near $\varDelta_1 = 0$ according to $\rho_{10}^{(1)}$. Then, for FWM BGS [Fig. 3(b1)], the expression of the corresponding density matrixes related to the FWM processes is $\rho_{10}^{(3)}$. In the expression, the single and double-photon emissions are expressed by $\varGamma_{10} + \mathrm{i}\varDelta_1$ and $\varGamma_{30} + \mathrm{i}(\varDelta_1 - \varDelta_3)$, respectively. When $\varDelta_2$ is scanned at different $\varDelta_1$, the FWM BGS is also dressed by the terms $|G_{31}|^2/[\varGamma_{30} + \mathrm{i}(\varDelta_1 - \varDelta_3)]$ and $|G_2|^2/[\varGamma_{20} + \mathrm{i}(\varDelta_1 + \varDelta_2)]$, which can significantly affect the intensity of FWM BGS. As a result, as shown in Fig. 3(b1), the profile of the baselines shows that the FWM BGS is enhanced by the field E_3 related to the dressing term $|G_{31}|^2/[\varGamma_{30} + \mathrm{i}(\varDelta_1 - \varDelta_3)]$. Furthermore, a dip in each sub curve represents that the FWM BGS is suppressed due to the dressing effect of $\boldsymbol{E}_2$ satisfying the condition $\varDelta_1 + \varDelta_2 = 0$ according to the $|G_2|^2/[\varGamma_{20} + \mathrm{i}(\varDelta_1 + \varDelta_2)]$ in $\rho_{10}^{(3)}$. The deepest dip appears at $\varDelta_2 = -\varDelta_1 = -\varDelta_3$ corresponding to the strongest PTS as shown in Fig. 3(b1).

Moreover, because the FLS is composed of two components: the single-photon fluorescence R_0 related to matrix element $\rho_{11}^{(2)}$ and the two-photon fluorescence R_1 related to matrix element $\rho_{22}^{(4)}$, so that every FLS appears as a dip containing a sharp peak on each base line as shown in Fig. 3(c1). In Fig. 3(c1), the heights of the baselines represent the intensity of the fluorescence R_0 at corresponding $\varDelta_1$, which is enhanced by the beam $E_3(E_3')$ near $\varDelta_1 = 0$ according to $|G_{31}|^2/[\varGamma_{30} + \mathrm{i}(\varDelta_1 - \varDelta_3)]$ in $\rho_{11}^{(2)}$. The baseline at $\varDelta_1 = 0$ is enhanced to the maximum height by the beam $E_3(E_3')$. The dips lower than the baseline show that the FLS R_0 is suppressed again by the beam E_2 at $\varDelta_2 = -\varDelta_1$ according to $|G_2|^2/[\varGamma_{20} + \mathrm{i}(\varDelta_1 + \varDelta_2)]$ in $\rho_{11}^{(2)}$. The suppression dips become shallow near $\varDelta_1 = 0$ due to the strong interaction between E_2 and E_3 according to $\rho_{11}^{(2)}$. In addition, the two-photon fluorescence R_1 related to the matrix element $\rho_{22}^{(4)}$ and every FLS has a sharp peak on each base line. It reaches its smallest at $\varDelta_1 = 0$ because of the strongest dressing effect of G_2 according to $|G_2|^2/[\varGamma_{20} + \mathrm{i}(\varDelta_1 + \varDelta_2)]$ in $\rho_{22}^{(4)}$. The corresponding theoretical simulation of PTS,

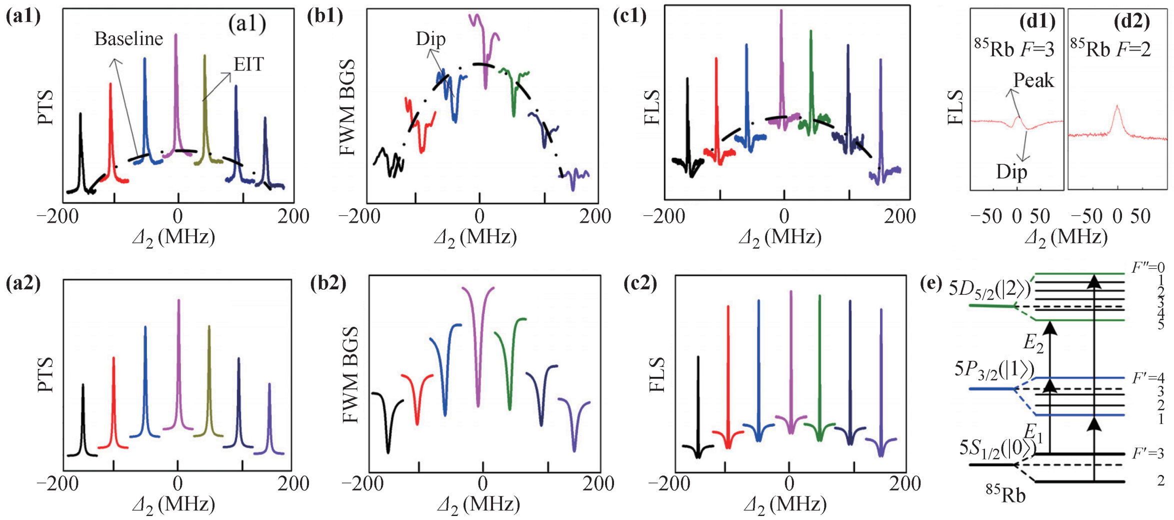

Fig. 3 Measured PTS **(a1)**, **(b1)** FWM BGS, and **(c1)** FLS versus Δ_2 at different discrete Δ_1. The values of Δ_1 are 180 MHz, 120 MHz, 60 MHz, 0 MHz, –60 MHz, –120 MHz, and –180 MHz from left to right. **(a2–c2)** are the calculated results of (a1)–(c1), respectively. **(d)** Measured FLS versus Δ_2 at the condition $\Delta_1 + \Delta_2 = 0$ with different hyperfine levels ^{85}Rb $F = 3$ and ^{85}Rb $F = 2$. **(e)** The energy level diagram shows the hyperfine levels of each driven state corresponding to (d). We set the power of E_1 is 2.3 mW, E_2 is 2.0mW, E_3 is 7.0 mW, and E_3' is 7.0 mW.

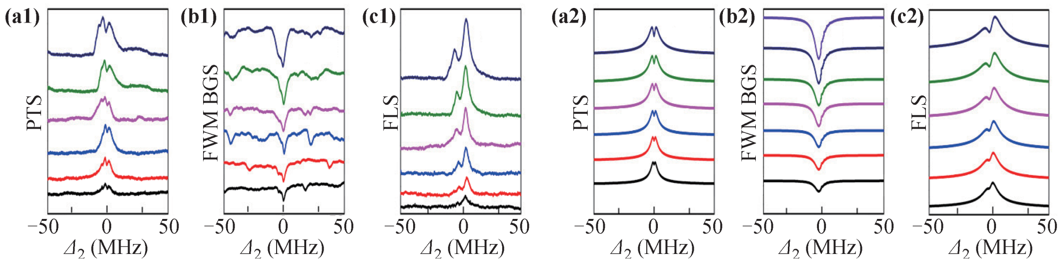

Fig. 4 Measured **(a1)** PTS, **(b1)** FWM BGS, and **(c1)** FLS versus Δ_2 and we set the power of E_2 as 5.1 mW, 9.2 mW, 13.0 mW, 17.1 mW, 21.6 mW, and 25.7 mW from bottom to top. The ground-state hyperfine level is $5S_{1/2}$ $F = 2(^{85}\text{Rb})$. **(a2–c2)** are the calculation results of (a1)–(c1).

FWM, and FLS are shown in Figs. 3(a2), (b2) and (c2), respectively, which are in good agreement with our experimental results.

Finally, we study the dressed FLS by scanning Δ_2 with the condition $\Delta_1 + \Delta_2 = 0$ under different ground-state hyperfine levels $5S_{1/2}F = 3$ of ^{85}Rb and $5S_{1/2}F = 2$ of ^{85}Rb in Fig. 3(d). The FLS for ground states $5S_{1/2}F = 3$ [Fig. 3(d1)] and $5S_{1/2}F = 2$ [Fig. 3(d2)] are different. One can see a peak on the baseline in Fig. 3(d2), but in Fig. 3(d1) we can see a peak in a dip, which is the sum of the second-order and the fourth-order FLS ($\rho_{11}^{(2)} + \rho_{22}^{(4)}$) on the baseline for the ground state $|0\rangle(5S_{1/2})F = 3$. The suppression dip is the R_0 according to $\rho_{11}^{(2)}$ in Fig. 3(d1), which means the dressing effect from E_2 in Fig. 3(d1) is stronger than that in Fig. 3(d2). Meanwhile, the peak in Fig. 3(d1) is lower than in Fig. 3(d1). The FLS in Fig. 3(d2) is the sum of ($\rho_{11}^{(2)} + \rho_{22}^{(4)}$) and the dressing effect by E_2 is considerably weaker and the dressing dip even disappears. These discrepancies could be explained with different transition dipole moments for $|0\rangle(5S_{1/2})F = 3 \to |1\rangle(5P_{3/2})F' = 4$ and $|0\rangle(5S_{1/2})F = 2 \to |1\rangle(5P_{3/2})F' = 1$. Figure 3(e) shows the hyperfine levels of each driven state corresponding to (d), from that we can obtain that the relative transition dipole moment is 3/2 by the frequency transition $|0\rangle(5S_{1/2})F = 3 \to |1\rangle(5P_{3/2})F' = 4$, which is larger than that in $|0\rangle(5S_{1/2})F = 2 \to |1\rangle(5P_{3/2})F' = 1$.

The powers of the dressing field E_2 can also affect the shape and intensity of PTS, FWM BGS, and FLS as shown in Figs. 4(a1)–(c1), and the ground-state hyperfine level is $5S_{1/2}F = 2(^{85}\text{Rb})$. Therefore, we concentrate on the power dependence of the measured signals by scanning Δ_2 with a fixed $\Delta_1 = 0$ when laser beams E_1, E_2, E_3, and E_3' are all turned on. First, as shown in Fig. 4(a1), the PTS is characterized by one small dip and two peaks. This experimental phenomenon can be

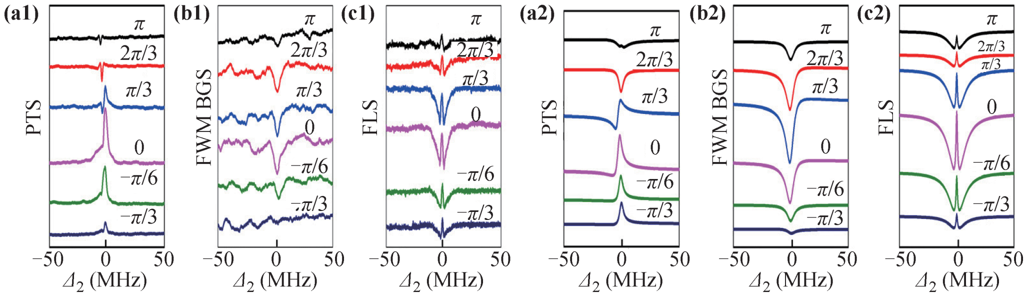

Fig. 5 **(a1–c1)** are respective PTS, FWM BGS, and FLS versus Δ_2 with ϕ_2 set at $\phi_2 = -\pi/3$, $\phi_2 = -\pi/6$, $\phi_2 = 0$, $\phi_2 = \pi/3$, $\phi_2 = 2\pi/3$ and $\phi_2 = \pi$ from bottom to top. The ground-state hyperfine level is $5S_{1/2}F = 3(^{85}\mathrm{Rb})$. **(a2–c2)** are the calculation results according to (a1)–(c1), and the field E_1 is 2.3 mW, E_2 is 20 mW, E_3 is 7.0 mW and E_3' is 7.0 mW.

attributed to the dressing term $|G_2|^2/[\Gamma_{20} + \mathrm{i}(\Delta_1 + \Delta_2)]$ induced by the field E_2 in $\rho_{10}^{(1)}$ when Δ_2 is scanned.

When the power of each light field is changed, the factor G_i can be changed, so the transmission signal and the reflection signal can be increased or decreased. However, with an increase of E_2 from the bottom to top, the dip of the PTS becomes obviously deeper as the dressing effect of E_2 is increased, and the height of the EIT peak becomes higher and is proportional to the dressing term $|G_2|^2/d_2$ in $\rho_{10}^{(1)}$. Specifically, it is clear that the spacing of the two peaks increases gradually from bottom to top as depicted in Figs. 4(a1). In Fig. 4(b1), the baselines represent the intensity of the FWM BGS. A dip in the baseline shows the suppression of the FWM BGS signal due to the second level dressing effect of E_2 according to the term $|G_2|^2/\mathrm{i}(\Delta_1 + \Delta_2) + \Gamma_{20}$ in $\rho_{10}^{(3)}$. The dip becomes deeper with increasing P_2 due to the enhanced dressing effect of E_2. A deeper dip indicates a decrease in reflected FWM BGS. When the power of E_2 is 25.7 mW in Fig. 4(b1), it is clear that the deepest dip can be obtained in the first curve from top to bottom. Finally, for similar reason, for FLS in Fig. 4(c1), the peak becomes obviously higher with P_2 increasing from bottom to top. This mainly results from the dressing field E_2 according to $\rho_{22}^{(4)}$. The experimental results agree with the theoretical simulation [Figs. 4(a2)–(c2)] very well.

Finally, similar to Fig. 3(c1), the FLS in Fig. 4(c1) is the sum of the second-order and fourth-order $(\rho_{11}^{(2)} + \rho_{22}^{(4)})$ on the baseline for ground state $|0\rangle(5S_{1/2})F = 2$. Comparing the FLS in Fig. 3(c1) and the FLS in Fig. 4(c1), we also can find the difference in the dip R_0 disappears because of the weak dressing effect according to $\rho_{11}^{(2)}$ in Fig. 3(c1), and the transition dipole moment in $|0\rangle(5S_{1/2})F = 2 \to |1\rangle(5P_{3/2})F' = 1$ is smaller than that in $|0\rangle(5S_{1/2})F = 3 \to |1\rangle(5P_{3/2})F' = 4$.

In this section, we focus on the variation of the measured signals by changing the phase ϕ_2 of the dress field E_2. The PTS [Fig. 5(a1)], FWM BGS [Fig. 5(b1)], and FLS [Fig. 5(c1)] are depicted simultaneously with the deflection phase ϕ_2 set at typical values. Here, ϕ_2 connects with the angle between the beam E_1 and E_2, and it could be manipulated by the orientations of induced dipole moments. The introduced phase factor ϕ_2 is related with the changed orientation of the induced dipole moment μ_2 by E_2, because of the modified angle between the directions of E_1 and E_2, as shown in Fig. 1(b). Correspondingly, the dressed PTS, FWM BGS, and PTS are proportional to $1/[d_1 + |G_2|^2 \mathrm{e}^{\mathrm{i}\phi_2}/d_2]$ [22], which can also be controlled by ϕ_2. The $\rho_{10}^{(1)}$, $\rho_{10}^{(3)}$, $\rho_{11}^{(2)}$, and $\rho_{22}^{(4)}$ can be modified as follows:

$$\rho_{10}^{(1)} = \mathrm{i}G_1/[d_1 + |G_{31}|^2/d_3 + |G_2|^2 \mathrm{e}^{\mathrm{i}\phi_2}/d_2] \tag{3}$$

$$\rho_{10}^{(3)} = \mathrm{i}G_1 G_3 G_3'/[d_1 + |G_{31}|^2/d_3 + |G_2|^2 \mathrm{e}^{\mathrm{i}\phi_2}/d_2] \tag{4}$$

$$\rho_{11}^{(2)} = -|G_1|^2/[\Gamma_{11}(d_1 + |G_{31}|^2/d_3 + |G_2|^2 \mathrm{e}^{\mathrm{i}\phi_2}/d_2)] \tag{5}$$

$$\rho_{22}^{(4)} = |G_1|^2 |G_2|^2/[\Gamma_{22} d_1 d_4 (d_2 + |G_2|^2 \mathrm{e}^{\mathrm{i}\phi_2}/d_1)] \tag{6}$$

We first show the evolutions of the PTS under phase ϕ_2 as shown in Fig. 5(a1). EIT in the PTS [Fig. 5(a1)] can be switched to EIA gradually along with ϕ_2. With ϕ_2 gradually varying from $-3/\pi$ to π, EIT becomes weaker and finally disappears, displayed in the Fig. 5(a1), while the EIA (dip lower than the baseline) arises and becomes strong. During this process, the strongest EIT and EIA individually appear at $\phi_2 = 0$ and $\phi_2 = -2\pi/3$. Depending on whether ϕ_2 is greater than or less than $\pi/3$, the PTS behaves mainly EIT or EIA. Therefore, from bottom to top, with the phase ϕ_2 turned from negative to positive, the PTS is converted from EIT to partial-EIT-partial-EIA and lastly to EIA.

Furthermore, relatively dressing FWM BGS in Fig. 5(b1) and the two-photon FLS R_1 in Fig. 5(c1), emerges as the peak on the background of single photon FLS R_0 and are obtained due to an enhanced nonlinear process. However, the deepest suppressed dips in FWM BGS and FLS R_0 appear at $\phi_2 = 0$ as shown in Fig. 5(b1). Suppression of the FWM BGS is demonstrated because of the dressing term $|G_2|^2/\mathrm{i}(\Delta_1 + \Delta_2) + \Gamma_{20}$ in $\rho_{10}^{(3)}$. For FLS [Fig. 5(c1)], the dip of the second-order R_0 induced by $\boldsymbol{E}_2$

gets deepest at $\phi_2 = 0$ due to the strongest EIT, one can see that the dressing dip can be changed from shallow to deeper then return to shallow from top to bottom. While the fourth-order peak R_1 gets strongest at $\phi_2 = 2\pi/3$ due to the largest EIA. Therefore, both the FWM BGS and FLS R_0 are significantly strengthened in company with the variation of the PTS as $\phi_2 = 2\pi/3$ and $\phi_2 = \pi$, respectively, as shown in Fig. 5(a1). The corresponding theoretical simulation of PTS, FWM, and FLS are shown in Figs. 5(a2), (b2) and (c2), respectively, which are in good agreement with our experimental results.

4 Conclusion

In summary, we experimentally and theoretically observed the PTS, FWM BGS, and FLS in the reverse-Y energy level system. These three types of signals can be controlled by the frequency detunings, the powers and the relative phases of the dressing beam E_2. We also find that with the switch between EIT and EIA in PTS, the suppression of FWM can be controlled by the phase ϕ_2 changing from 0 to $-\pi$. We can make use of the phase-regulated switch in a non-linear optical device like an optical switch and optical wavelength convertor. In addition, we observe the similarities and discrepancies between the two ground-state hyperfine levels $|0\rangle(5S_{1/2})F = 2$ and $|0\rangle(5S_{1/2})F = 3$ of Rb 85 for the first time. Such research could be applicable in optical amplifiers and quantum information processing.

Acknowledgements This work was supported by the national Basic Research Program of China (973 Program) (Grant No. 2012CB921804), KSTIT of Shaanxi province (Grant No. 2014KCT-10), and the National Natural Science Foundation of China (Grant Nos. 11474228 and 61308015).

References

1. J. Gea-Banacloche, Y. Li, S. Jin, and M. Xiao, Electromagnetically induced transparency in ladder-type inhomogeneously broadened media: Theory and experiment, *Phys. Rev. A* 51(1), 576 (1995)
2. K. J. Boller, A. Imamolu, and S. E. Harris, Observation of electromagnetically induced transparency, *Phys. Rev. Lett.* 66(20), 2593 (1991)
3. M. D. Lukin, A. B. Matsko, M. Fleischhauer, and M. O. Scully, Quantum noise and correlations in resonantly enhanced wave mixing based on atomic coherence, *Phys. Rev. Lett.* 82(9), 1847 (1999)
4. H. Kang, G. Hernandez, and Y. Zhu, Resonant four-wave mixing with slow light, *Phys. Rev. A* 70(6), 061804 (2004) (R)
5. M. Jain, H. Xia, G. Y. Yin, A. J. Merriam, and S. E. Harris, Efficient nonlinear frequency conversion with maximal atomic coherence, *Phys. Rev. Lett.* 77(21), 4326 (1996)
6. P. R. Hemmer, D. P. Katz, J. Donoghue, M. S. Shahriar, P. Kumar, and M. Cronin-Golomb, Efficient low-intensity optical phase conjugation based on coherent population trapping in sodium, *Opt. Lett.* 20(9), 982 (1995)
7. X. M. Liu, Broad and tunable multi-wavelength fiber laser at the assistance of modulation-instability-assisted four-wave mixing, *Laser Phys.* 20(4), 842 (2010)
8. X. M. Liu, X. Q. Zhou, and C. Lu, Four-wave mixing assisted stability enhancement: theory, experiment, and application, *Opt. Lett.* 30(17), 2257 (2005)
9. X. M. Liu, Theory and experiments for multiple four-wave-mixing processes with multifrequency pumps in optical fibers, *Phys. Rev. A* 77(4), 043818 (2008)
10. J. W. Gao, Y. Zhang, N. Ba, C. L. Cui, and J. H. Wu, Dynamically induced double photonic bandgaps in the presence of spontaneously generated coherence, *Opt. Lett.* 35(5), 709 (2010)
11. M. Artoni and G. C. La Rocca, Optically tunable photonic stop bands in homogeneous absorbing media, *Phys. Rev. Lett.* 96(7), 073905 (2006)
12. Z. K. Wu, K. G. Chang, Y. Hu, Y. Z. Zhang, Z. H. Jiang, and Y. P. Zhang, Modulation of four-wave mixing via photonic band gap, *Front. Phys.* 9(5), 665 (2014)
13. Z. G. Wang, M. Q. Gao, Z. Ullah, H. X. Chen, D. Zhang, Y. Q. Zhang, and Y. P. Zhang, Optical processes in different types of photonic band gap structures, *Opt. Mater.* 44, 58 (2015)
14. Y. Zhang, C. Yuan, Y. Zhang, H. Zheng, H. Chen, C. Li, Z. Wang, and M. Xiao, Surface solitons of four-wave mixing in an electromagnetically induced lattice, *Laser Phys. Lett.* 10(5), 055406 (2013)
15. Z. K. Wu, Y. Q. Zhang, T. K. Liu, Z. Y. Zhang, C. Li, Y. P. Zhang, and M. Xiao, Coherent control of dressed images of four-wave mixing, *Front. Phys.* 8(2), 228 (2013)
16. J. H. Wu, M. Artoni, and G. C. La Rocca, Controlling the photonic band structure of optically driven cold atoms, *J. Opt. Soc. Am. B* 25(11), 1840 (2008)
17. Y. Zhang, Z. Wu, M. R. Belić, H. Zheng, Z. Wang, M. Xiao, and Y. Zhang, Photonic Floquet topological insulators in atomic ensembles, *Laser Photonics Rev.* 9(3), 331 (2015)
18. Z. Ullah, Z. G. Wang, M. Q. Gao, D. Zhang, Y. Q. Zhang, H. Gao, and Y. P. Zhang, Observation of the four wave mixing photonic band gap signal in electromagnetically induced grating, *Opt. Express* 22(24), 29544 (2014)
19. A. W. Brown and M. Xiao, All-optical switching and routing based on an electromagnetically induced absorption grating, *Opt. Lett.* 30(7), 699 (2005)
20. C. Liu, Z. Dutton, C. Behroozi, and L. Hau, Observation of coherent optical information storage in an atomic medium using halted light pulses, *Nature* 409(6819), 490 (2001)
21. G. Wang, H. Lu, and X. Liu, Dispersionless slow light in MIM waveguide based on a plasmonic analogue of electromagnetically induced transparency, *Opt. Express* 20, 902 (2012)
22. D. Zhang, Z. G. Wang, M. Gao, Z. Ullah, Y. Q. Zhang, H. X. Chen, and Y. P. Zhang, Observation of triple-dressing on photonic band gap of optically driven hot atoms, *J. Opt. Soc. Am. B* 32(9), 1961 (2015)
23. Z. G. Wang, P. Ying, P. Y. Li, H. Y. Lan, H. Q. Huang, H. Tian, J. P. Song, and Y. P. Zhang, Phase regulated suppression and enhancement switches of four-wave mixing and fluorescence, *Front. Phys.* 9(2), 153 (2014)